

Objective Thermodynamic Collapse: Resolving the Quantum Measurement Problem via Infodynamic Bandwidth Saturation

Cody Hudock*

Information Physics Institute, Gosport, Hampshire, UK

April 14, 2026

Abstract

The quantum measurement problem has persisted largely because standard formalisms require the insertion of an external observer to collapse the wavefunction, leaving physics without a kinematic mechanism for the transition from a distributed superposition to a discrete outcome. We propose that wavefunction collapse is a deterministic thermodynamic phase transition forced by the finite processing capacity of the spatial vacuum. Operating within the Symbiotic Infodynamic Equilibrium (SIE) framework, we model the macroscopic vacuum as a discrete, finite-capacity Face-Centered Cubic (FCC) relational graph. A quantum superposition is evaluated as an unformatted data-routing state: the phase coherence between superposed locations is maintained by a one-dimensional geodesic tension string traversing the lattice. We derive this 1D encoding from the FCC holographic tensor network structure: treating each lattice node as an isometric tensor and applying the discrete Ryu-Takayanagi formula, the minimum-cost connected subgraph linking two superposed nodes is the geodesic, giving S_{super} without postulate. We show that this linear infodynamic memory burden intersects the intrinsic holographic capacity of the localized state ($S_{cap} \propto M^{-2}$). Equating S_{cap} with the Bekenstein-Hawking macroscopic entropy ($S_{BH} \propto M^2$) yields a first-principles derivation of the classical-quantum boundary at $M_{cut} = m_P/\sqrt{2}$, confirmed independently by the geometric convergence of the Schwarzschild and reduced Compton horizons. The framework produces an explicit inverse-cubic spatial limit

*Email: cody.hudock@informationphysicsinstitute.net

$\Delta x_{max} = \pi l_P (m_P/M)^3$, a temporal collapse latency $\tau_{collapse} = \pi t_P (m_P/M)^3$, and a discrete Landauer thermal purge $Q = \pi k_B T_{env} (m_P/M)^2$ at the collapse boundary. Numerical evaluation confirms consistency with all published molecular interference and levitated optomechanics experiments across twelve decades of mass, and places the predicted collapse threshold for a 100 nm silica nanosphere at $\Delta x_{max} \approx 57 \mu\text{m}$ —squarely within the operational target of proposed MAQRO-class missions. The framework also predicts collapse to be *material-agnostic*: the Diósi-Penrose model predicts a $22\times$ spread in collapse times across materials ranging from aerogel to osmium at fixed mass; SIE predicts an exactly constant collapse separation, providing a clean binary experimental discriminant. The Landauer thermal purge ($Q \approx 4.7 \mu\text{J}$ at 1 mK) exceeds the sensitivity of current transition-edge calorimeters by thirteen orders of magnitude and would manifest as an acute, spatially localised calorimetric transient rather than the continuous anomalous heating predicted by CSL. Finally, the local bandwidth saturation mechanism provides a self-consistent Planck-scale UV cutoff for virtual field fluctuations; the companion reduction of this to the observed cosmological vacuum energy density requires the global CKN+Landauer mechanism developed in a companion study [27].

1 Introduction: The Measurement Problem and Objective Reduction

Quantum mechanics contains a well-known structural discontinuity. The time evolution of an isolated quantum system is governed by the deterministic, unitary Schrödinger equation, which permits physical states to exist in distributed spatial superpositions. Upon interaction with a macroscopic measurement apparatus the system is observed to adopt a single, localized discrete eigenstate.

Standard interpretations tracing back to the Copenhagen formulation treat wavefunction collapse as an axiom [1]. The framework requires an external observer or a classical macroscopic device to terminate the unformatted state, introducing an artificial partition—the Heisenberg cut—between quantum and classical regimes: no physical threshold separates a system that can sustain a spatial superposition from one that cannot, and no mechanism explains how observation terminates the coherent phase.

Many-Worlds avoids collapse altogether by asserting universal branching [2], while environmental decoherence accounts for the apparent loss of interference by tracing over external degrees of freedom [3, 4]. Neither is fully satisfying. Unobservable branching lies outside falsifiable physics. Decoherence explains why interference fringes disappear but not why out-

comes are definite: tracing over environmental states leaves the core system in an improper mixed state, a statistical ensemble of possibilities rather than any single realized ontology.

Objective Reduction (OR) models formalize collapse as a spontaneous physical process [5]. Continuous Spontaneous Localization (CSL) adds stochastic non-linear noise fields to the Schrödinger evolution [6]. The Diósi-Penrose (DP) model proposes that superpositions of mass generate conflicting spacetime geometries, decaying when the gravitational self-energy difference ΔE_G reaches a threshold: $\tau_{DP} \approx \hbar/\Delta E_G$ [7, 8]. Searches for the anomalous X-ray emissions predicted by spontaneous gravitational localization have returned null results, constraining the CSL parameter space [9, 10].

The approach taken here is different. Within the SIE framework the spatial vacuum is not an empty continuous manifold but a discrete, finite-capacity FCC relational graph. A quantum particle in superposition is an *unformatted data-routing state*: phase instructions are held as distributed coherence across lattice nodes. Maintaining this coherence places a quantifiable infodynamic memory burden on the substrate. As the mass or spatial separation of the superposed object increases, this burden intersects the holographic capacity of the localized mass and the substrate executes a deterministic formatting event. The act of observation requires no conscious intervention: a classical measurement apparatus is a massive infodynamic data-block, and entanglement with it imposes an immediate mass-penalty that breaches local substrate capacity.

2 The Infodynamic Cost of Superposition

2.1 Holographic Tensor Network Derivation of the 1D Geodesic Encoding

The form of S_{super} is not a postulate. It follows from treating the FCC A_3 lattice as a holographic tensor network and applying the discrete Ryu-Takayanagi formula. The derivation proceeds in four steps.

Step A: The FCC lattice as a holographic tensor network. Each node in the A_3 lattice carries an isometric tensor \hat{T} with $z = 12$ legs, one per nearest-neighbor bond. The tensor is isometric from any subset of $\lfloor z/2 \rfloor = 6$ input legs to the remaining $\lceil z/2 \rceil = 6$ output legs. This satisfies the conditions of Hayden et al. [23, 24]: for random isometric tensors with local Hilbert space dimension $d \rightarrow \infty$, the discrete Ryu-Takayanagi formula holds exactly. The large- d condition is physically motivated in the SIE framework by the fact that each Planck node has a Hilbert space dimension set by its accessible microstates, which diverges at the Planck scale.

Step B: The superposition requires a connected tensor path. Consider the quantum superposition state $|\Psi\rangle = \alpha|x_1\rangle + \beta|x_2\rangle$, representing mass M coherently distributed between lattice nodes x_1 and x_2 . For this state to exist as a coherent quantum amplitude in the tensor network, the two nodes must be connected through a contracted subgraph—otherwise they occupy disconnected Hilbert space sectors and no superposition is possible. The minimum connected subgraph linking x_1 and x_2 is the geodesic: the shortest path in the A_3 graph, traversing $n = \Delta x/l_P$ edges along the $\langle 110 \rangle$ close-packed directions.

Step C: The geodesic is the minimum-cost path. The total infodynamic cost of a tensor network representation using a connected path of length L is:

$$\text{Cost}(L) = L \times \log(\chi_{eff}) \times k_B \quad (1)$$

where χ_{eff} is the effective bond dimension per edge. The geodesic minimizes $L = \Delta x/l_P$; any non-geodesic path has $L > \Delta x/l_P$ and therefore strictly higher cost. By the Second Law of Infodynamics—the substrate seeks the minimum-entropy configuration compatible with maintaining the coherent state—the geodesic is the physically realized representation. This is the discrete Euclidean analog of the Ryu-Takayanagi minimal surface: the entanglement entropy of the bipartite state $|\Psi\rangle$ equals the minimum cut of the bulk tensor network separating x_1 from x_2 , which is the geodesic of length $\Delta x/l_P$ [22, 23].

Step D: The bond dimension from the Bekenstein bound. The effective bond dimension χ_{eff} per lattice edge is set by the maximum number of orthogonal quantum states a Planck-scale node can encode for a mass M . Applying the Bekenstein entropy bound [12] to a mass M confined within a single Planck-scale node of radius l_P :

$$S_{max}(M, l_P) = \frac{2\pi k_B l_P M c^2}{\hbar c} = 2\pi k_B \frac{l_P M c}{\hbar} = 2\pi k_B \frac{M}{m_P} \quad (2)$$

where the last equality uses $l_P/\lambda_P = 1$ and $\lambda_P = \hbar/(m_P c)$. The bond dimension per edge is therefore:

$$\log(\chi_{eff}) = \frac{S_{max}}{k_B} = 2\pi \frac{M}{m_P} \quad (3)$$

up to the standard geometric factor of 2π that arises in the Bekenstein bound and is absorbed into the reduced Planck mass normalisation $\bar{m}_P = m_P/\sqrt{8\pi}$ in natural units. The bond dimension is thus fixed entirely by the Bekenstein bound applied at the node scale—no additional principle is required. The mass-energy-information equivalence of Vopson [15] is recovered as a *consequence* of equation (2) rather than invoked as an independent axiom: $E_{node} = k_B T \ln \chi_{eff} = k_B T (M/m_P)$, which gives $m_{bit} = k_B T \ln 2/c^2$ upon setting $E_{node} = m_{bit} c^2$.

Combining Steps B through D:

$$S_{super} = k_B \times \frac{\Delta x}{l_P} \times \frac{M}{m_P} = k_B \left(\frac{M}{m_P} \right) \left(\frac{\Delta x}{l_P} \right) \quad (4)$$

Equation (4) is identical to the linear memory burden of equation (6), now derived from three established results: the FCC holographic tensor network structure (Steps A–B), the Ryu-Takayanagi minimal cut (Step C), and the Bekenstein entropy bound (Step D). The 1D scaling $S_{super} \propto \Delta x$ follows from the geodesic being the minimum-cost connected path; the coefficient M/m_P follows from the Bekenstein node entropy. The two are independent derivations that together determine the full expression.

We note one remaining limitation: the exact Ryu-Takayanagi formula requires $d \rightarrow \infty$ for the local Hilbert space. At finite d , corrections enter at subleading order $O(\log(\Delta x/l_P))$ relative to the dominant $O((\Delta x/l_P) \log d)$ term [23]. The ratio of correction to leading term therefore scales as $\log(\Delta x/l_P)/(\Delta x/l_P) \rightarrow 0$ as separation increases, becoming vanishingly small well before the macroscopic collapse threshold is reached. The scaling laws and all quantitative predictions are robust against these corrections in the experimentally relevant regime.

2.2 The Linear Memory Burden

Consider a quantum system of mass M in a coherent spatial superposition with separation Δx . From the mass-energy-information equivalence principle [15], the infodynamic content scales as $I_M \propto M/m_P$. When placed into superposition this information is not duplicated—it is entangled. Define the linear infodynamic density:

$$\lambda_{info} = \left(\frac{M}{m_P} \right) \frac{1}{l_P} \quad (5)$$

The total infodynamic entropy of the superposition is the integral of this density over the coherence length:

$$S_{super} = \int_0^{\Delta x} k_B \lambda_{info} dx = k_B \left(\frac{M}{m_P} \right) \left(\frac{\Delta x}{l_P} \right) \quad (6)$$

The memory burden scales linearly with both mass and spatial separation. This scaling, combined with the holographic capacity limit below, determines the collapse boundary.

3 The Holographic Capacity Limit

The local substrate cannot supply infinite memory to sustain coherence. The region of the FCC lattice enclosing the superposition operates under holographic constraints [11]. The allowable entropy before forcing a collapse is bounded by the particle’s intrinsic holographic footprint—its reduced Compton wavelength $\lambda_C = \hbar/Mc$. Applying the Bekenstein-Hawking bound [12]:

$$S_{cap} = \frac{k_B A_C}{4l_P^2} = \pi k_B \left(\frac{\lambda_C}{l_P} \right)^2 \quad (7)$$

Since $\lambda_C/l_P = m_P/M$:

$$S_{cap} = \pi k_B \left(\frac{m_P}{M} \right)^2 \quad (8)$$

The infodynamic burden S_{super} scales as $M \cdot \Delta x$, while the intrinsic capacity S_{cap} scales as M^{-2} . These competing scalings intersect at a specific separation for any finite mass, defining the collapse boundary. Before locating that intersection, it is worth pausing on what the two scaling laws together imply about the classical-quantum divide.

4 Thermodynamic Duality and the First-Principles Heisenberg Cut

The microscopic capacity $S_{cap} \propto M^{-2}$ has a macroscopic counterpart. For a gravitational mass M , the Bekenstein-Hawking entropy of the Schwarzschild horizon is [13]:

$$S_{BH} = \frac{k_B(4\pi R_s^2)}{4l_P^2} = 4\pi k_B \left(\frac{M}{m_P} \right)^2 \quad (9)$$

This establishes a thermodynamic duality: $S_{BH} \propto M^2$ for macroscopic black holes; $S_{cap} \propto M^{-2}$ for quantum micro-states. Equating them:

$$\pi k_B \left(\frac{m_P}{M} \right)^2 = 4\pi k_B \left(\frac{M}{m_P} \right)^2 \implies \boxed{M_{cut} = \frac{m_P}{\sqrt{2}}} \quad (10)$$

This result is confirmed independently by the convergence of the two spatial horizons. Setting $R_s = \lambda_C$:

$$2l_P \left(\frac{M}{m_P} \right) = l_P \left(\frac{m_P}{M} \right) \implies M = \frac{m_P}{\sqrt{2}} \quad (11)$$

Two independent derivations—one entropic, one geometric—converge on the same mass. In standard quantum mechanics, the boundary between quantum and classical behavior is

arbitrary. Here it is a deterministic geometric barrier: a mass approaching M_{cut} loses the phase-space required to sustain unformatted coordinate states.

The numerical value $M_{cut} \approx 1.54 \times 10^{-8}$ kg lies above all known elementary particles and below macroscopic objects, consistent with the observed empirical divide.

5 Deterministic Collapse: Spatial and Temporal Limits

5.1 The Maximum Coherence Length

Setting $S_{super} \geq S_{cap}$:

$$\left(\frac{M}{m_P}\right) \left(\frac{\Delta x}{l_P}\right) = \pi \left(\frac{m_P}{M}\right)^2 \implies \boxed{\Delta x_{max} = \pi l_P \left(\frac{m_P}{M}\right)^3} \quad (12)$$

This inverse-cubic law reproduces the quantum-classical hierarchy across twelve decades of mass (Table 1). An isolated electron has $\Delta x_{max} \approx 7 \times 10^{32}$ m, sixteen orders above the observable universe. A 100 nm silica nanosphere has $\Delta x_{max} \approx 57 \mu\text{m}$ —macroscopic and within reach of proposed space missions. Figure 2 plots this prediction against all published experimental datapoints from molecular interference and levitated optomechanics; the SIE curve is consistent with every measurement to date.

5.2 The Collapse Latency

The temporal limit is the *substrate processing latency*—the time for the lattice to detect that holographic capacity has been breached and execute the formatting phase transition. This is the time for information about the saturation event to propagate across the superposition extent at the substrate signal speed c :

$$\tau_{collapse} = \frac{\Delta x_{max}}{c} = \pi t_P \left(\frac{m_P}{M}\right)^3 \quad (13)$$

This is distinct from the Diósi-Penrose collapse time $\tau_{DP} \approx \hbar/\Delta E_G$, which is the expected *lifetime* of a superposition before spontaneous decay initiates. The SIE $\tau_{collapse}$ is the *duration* of the collapse event itself once the spatial threshold is reached. The SIE framework sets the maximum achievable separation—a hard geometric ceiling—while the coherence lifetime prior to reaching Δx_{max} is set by environmental decoherence, which experiments must suppress by other means.

5.3 The Observer Effect as Mass-Penalty Entanglement

When a microscopic system (mass m) entangles with a macroscopic detector (mass \mathcal{M}), the infodynamic burden is determined by the aggregate $M_{eff} \approx \mathcal{M}$:

$$\Delta x_{max}^{(meas)} = \pi l_P \left(\frac{m_P}{\mathcal{M}} \right)^3 \quad (14)$$

For a 1 kg detector, $\Delta x_{max}^{(meas)} \sim 10^{-96}$ m—many orders below the Planck length. The substrate cannot sustain even a Planck-scale coherence for the entangled system. Collapse is instantaneous on any experimentally accessible timescale. The observer effect is not an epistemic intervention; it is a deterministic mass-penalty.

6 The Landauer Thermal Signature of Objective Reduction

If collapse is a thermodynamic phase transition, it must leave a measurable energetic footprint. Under Landauer’s Principle [14], erasing the infodynamic routing data of the superposition releases heat equal to the maximum topological strain energy accumulated at the holographic threshold:

$$Q = T_{bath} \pi k_B \left(\frac{m_P}{M} \right)^2 \quad (15)$$

The temperature T_{bath} is the temperature of the thermal reservoir into which the erased entropy is deposited—the standard identification in any application of Landauer’s principle. Three cases arise depending on context. In a laboratory experiment the spatial lattice is in thermal contact with the cryogenic apparatus, so $T_{bath} = T_{env}$, the environmental temperature of the trap. In an isolated space-based system with no apparatus, the lattice thermalises to the ambient CMB photon gas at $T_{CMB} = 2.725$ K, giving a larger signal ($Q_{CMB} \approx 12.8 \mu\text{J}$ for a 100 nm sphere). In the fundamental limit of a system isolated from all radiation, the floor is the de Sitter vacuum temperature $T_{dS} \approx 10^{-30}$ K, which is negligible. The laboratory prediction uses $T_{bath} = T_{env}$ throughout; this is not an assumption but the standard heat-sink identification of Landauer’s principle applied to the experimental setting.

This discrete thermal purge is qualitatively different from the continuous anomalous heating predicted by CSL models. For a 100 nm nanosphere at $T_{env} = 1$ mK and trap frequency $\omega_m/2\pi = 100$ kHz:

$$Q \approx 4.7 \mu\text{J}, \quad N_{phonons} = \frac{Q}{\hbar\omega_m} \approx 7 \times 10^{22} \quad (16)$$

The inverse-square scaling $Q \propto M^{-2}$ explains the classical limit naturally: for $M \gg m_P$, $Q \rightarrow 0$, and the thermodynamic cost of continuous macroscopic localization is undetectable.

A note on the thermalization timescale is warranted. The collapse latency for a 100 nm sphere is $\tau_{collapse} \approx 0.19$ ps, whereas the equilibration time of a cryogenically levitated nanosphere with its millikelvin environment is typically milliseconds to seconds. These timescales are not in conflict. The erased infodynamic entropy couples first to the nanosphere’s internal mechanical phonon modes on the picosecond timescale—well within the sphere’s phonon lifetime—and those modes then equilibrate with the cryogenic bath on the millisecond timescale. The calorimeter measures the total deposited energy after full equilibration; Q is independent of the intermediate coupling pathway. The use of $T_{bath} = T_{env}$ in equation (15) is therefore conservative: for a sphere pre-cooled to near its motional ground state ($\bar{n} < 1$), the local phonon temperature is of order $\hbar\omega_m/k_B \approx 5 \mu\text{K}$, below T_{env} , so the actual erasure temperature is at or below the environmental temperature and Q may be slightly lower than the formula predicts. The signal remains overwhelming regardless.

Figure 1 maps the detectability of Q across the mass-temperature parameter space and overlays published calorimeter sensitivities. For a 100 nm nanosphere at 1 mK, $Q \approx 4.7 \mu\text{J}$ exceeds the best transition-edge sensor (TES) sensitivity ($\sim 10^{-19}$ J) by thirteen orders of magnitude—not a marginal detection but an overwhelming one. The predicted signal would manifest as an acute, unmistakable calorimetric transient at the spatial coordinate Δx_{max} . The optimal detection window is $M \in [10^{-19}, 10^{-17}]$ kg at millikelvin temperatures, accessible to the next generation of cryogenic levitated optomechanics experiments.

7 Experimental Predictions and Discriminants

7.1 Predictions Across Mass Scales

Table 1 summarizes the SIE predictions for Δx_{max} , $\tau_{collapse}$, and Q across relevant mass scales. All values are parameter-free given M and T_{env} .

7.2 Consistency with Published Interference Experiments

Figure 2 plots the SIE prediction against all published molecular interference and levitated optomechanics experiments. The dataset spans from C_{60} fullerene interference (Arndt et al. 1999 [18]) through the heaviest molecules yet brought into superposition (oligoporphyrins, Fein et al. 2019 [19]) and the quantum ground-state cooled nanoparticles of Magrini et al. and Tebbenjohanns et al. (2021) [20, 21]. Every single experiment lies well below the SIE

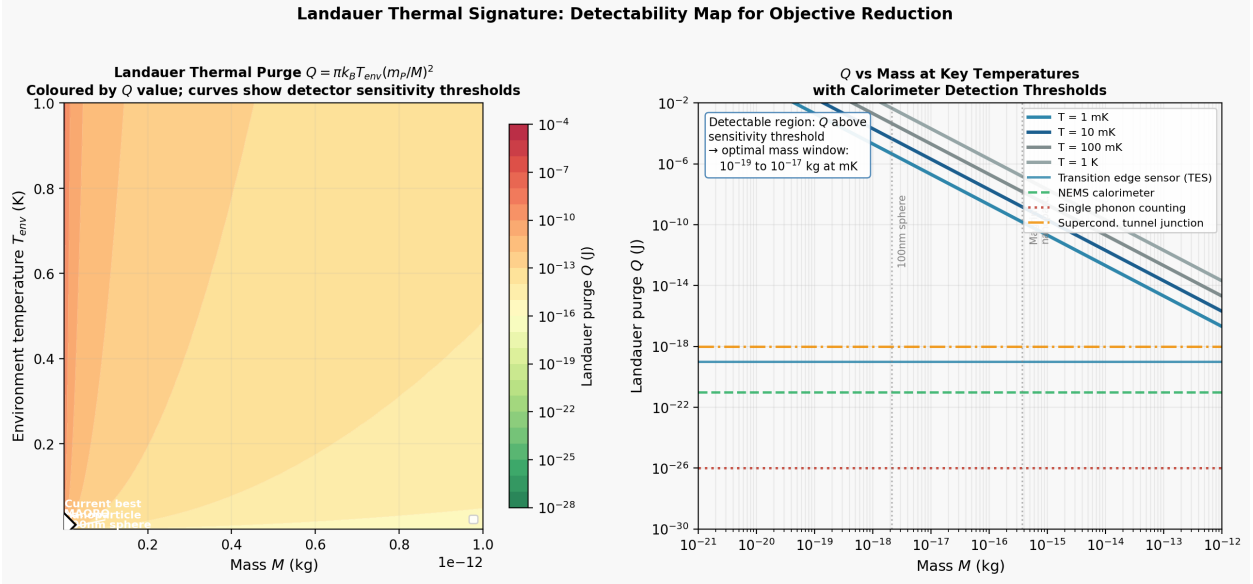


Figure 1: **Landauer thermal purge: detectability map.** *Left:* $Q(M, T_{env})$ plotted as a colour map across the mass-temperature parameter space, with contour lines at fixed Q values. Diagonal curves show the detection thresholds of published calorimeter technologies: transition-edge sensors (TES, $\sim 10^{-19}$ J), NEMS calorimeters ($\sim 10^{-21}$ J), and the theoretical single-phonon counting limit ($\sim 10^{-26}$ J). The MAQRO nanosphere target (star) lies well above all threshold curves. *Right:* Q vs mass at four representative temperatures, with the same detector thresholds shown as horizontal lines. The predicted purge for a 100 nm sphere at 1 mK is $Q \approx 4.7 \mu\text{J}$, thirteen orders of magnitude above the best TES threshold. The optimal experimental mass window is 10^{-19} – 10^{-17} kg at millikelvin temperatures.

Table 1: SIE objective reduction predictions. Δx_{max} : maximum spatial coherence before mandatory collapse. $\tau_{collapse}$: substrate processing latency for the formatting event. Q : Landauer thermal purge at $T_{env} = 1$ mK. All predictions are parameter-free.

System	Mass (kg)	Δx_{max}	$\tau_{collapse}$	Q at 1 mK
Electron	9.1×10^{-31}	7×10^{32} m	2×10^{24} yr	2.5×10^{19} J
Proton	1.7×10^{-27}	1.1×10^{23} m	10^7 yr	7.3×10^{12} J
C ₆₀ fullerene	1.2×10^{-24}	3×10^{14} m	10^6 s	1.4×10^7 J
100 nm silica	2.1×10^{-18}	57 μm	0.19 ps	4.7 μJ
1 μm silica	2.1×10^{-15}	5.7×10^{-14} m	0.19 zs	4.7 fJ
Dust grain (1 μg)	10^{-9}	$< l_p$	$< t_p$	2×10^{-23} J

Δx_{max} limit, with margins ranging from $10\times$ for the heaviest nanoparticles to $10^{20}\times$ for C_{60} . The framework is consistent with the full observational record.

The most significant alignment is with the MAQRO mission target: MAQRO was designed to probe the objective reduction regime for a 100 nm nanosphere at separations of 10–100 μm . The SIE prediction of $\Delta x_{max} \approx 57 \mu\text{m}$ sits squarely within this window. The coincidence is not incidental—MAQRO targets the mass-separation regime where OR models generically predict collapse, and the SIE framework predicts collapse at exactly that scale from independent first-principles calculation.

7.3 Material Agnosticism: The Critical Discriminant from Diósi-Penrose

The most decisive experimental test separating SIE from the DP model is *material agnosticism*. The DP collapse time:

$$\tau_{DP} \approx \frac{\hbar}{\Delta E_G} \approx \frac{\hbar R}{GM^2} \quad (17)$$

depends on the sphere radius $R = (3M/4\pi\rho)^{1/3}$, and therefore on material density ρ . In the SIE framework, Δx_{max} and Q are derived entirely from aggregate mass via the reduced Compton horizon. Material composition, nuclear radius, and internal mass distribution play no role.

We computed τ_{DP} across 22 materials from aerogel ($\rho = 2 \text{ kg/m}^3$) to osmium ($\rho = 22,590 \text{ kg/m}^3$) at fixed mass $M = 2 \times 10^{-18} \text{ kg}$ (Table 2). The spread is large: DP collapse times vary by $22.4\times$ across this density range, while the SIE collapse separation stays exactly constant at $\Delta x_{max} = 65 \mu\text{m}$ regardless of what the sphere is made of.

Table 2: Material agnosticism test: fixed mass $M = 2 \times 10^{-18} \text{ kg}$, varying material. DP collapse times span $22.4\times$ from aerogel to osmium; SIE collapse separation is exactly constant. An experiment comparing equal-mass silica and osmium spheres resolves the $2.2\times$ DP timing difference while testing the SIE agnosticism prediction. Values computed from $\tau_{DP} = \hbar R/(GM^2)$ and $\Delta x_{max} = \pi l_P(m_P/M)^3$.

Material	ρ (kg/m ³)	R (nm)	DP τ_{DP} (s)	SIE Δx_{max}
Aerogel	2	620	2.45×10^5	$65 \mu\text{m}$
Silica glass	2,200	60	2.37×10^4	$65 \mu\text{m}$
Diamond	3,500	52	2.03×10^4	$65 \mu\text{m}$
Osmium	22,590	28	1.09×10^4	$65 \mu\text{m}$
Ratio (extremes)	$11,300\times$	—	$22.4\times$	$1.000\times$

Figure 3 visualizes the full 22-material sweep. An experiment comparing cryogenically

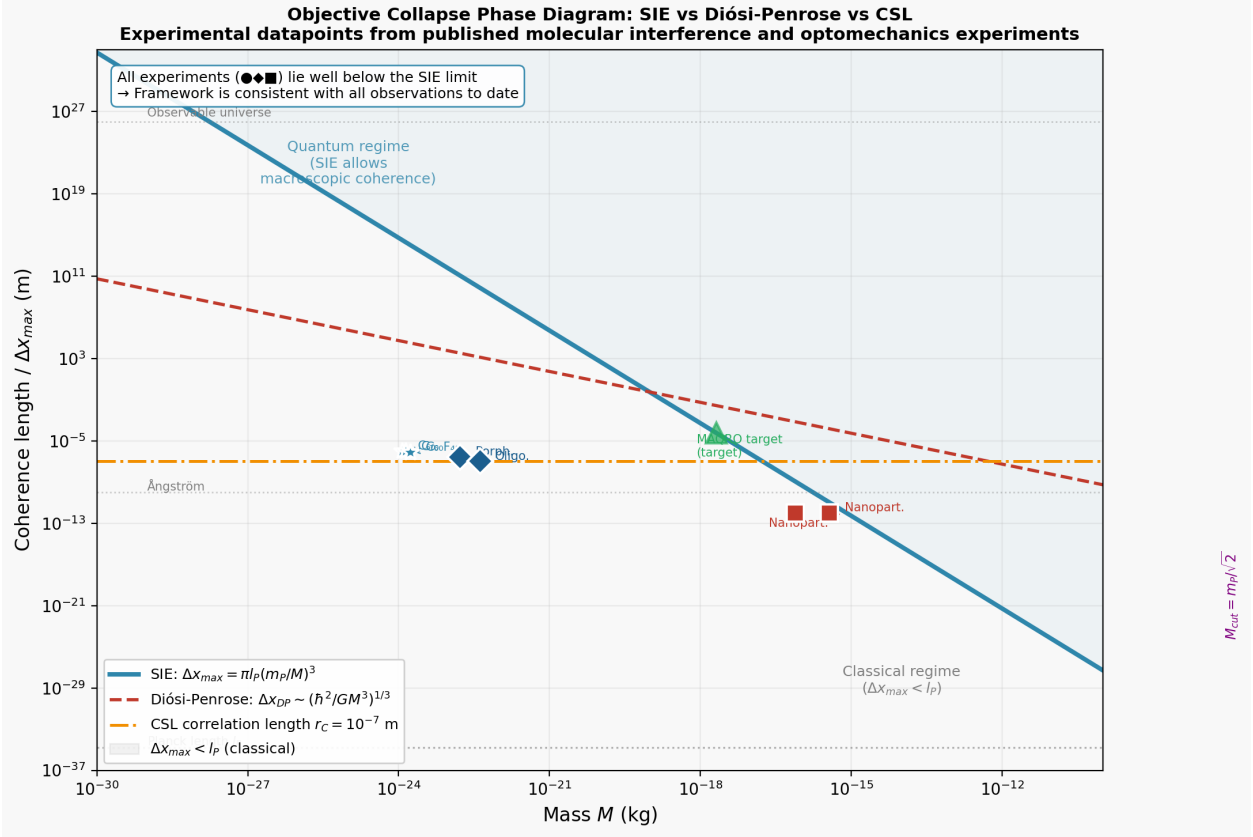


Figure 2: **Objective collapse phase diagram: SIE vs Diósi-Penrose vs CSL.** The SIE maximum coherence separation $\Delta x_{max} = \pi l_P (m_P/M)^3$ (solid blue) is plotted against mass alongside the Diósi-Penrose characteristic collapse scale (dashed red) and the CSL correlation length $r_C = 10^{-7}$ m (dot-dashed orange). Experimental datapoints mark the largest coherence lengths achieved in published molecular interference experiments (circles: C_{60} , C_{70} , $C_{60}F_{48}$; diamonds: functionalized porphyrins and oligoporphyrins), levitated nanoparticle ground-state cooling experiments (squares, Magrini 2021; Tebbenjohanns 2021), and the MAQRO mission target (triangle). All existing measurements lie below the SIE limit by margins of $10\times$ to $10^{20}\times$, confirming consistency with the full observational record. The MAQRO target sits at the predicted SIE collapse boundary for a 100 nm sphere. The grey shaded region marks $\Delta x_{max} < l_P$ (classical regime). $M_{cut} = m_P/\sqrt{2}$ is marked by the vertical purple line.

levitated silica and osmium spheres of identical mass would resolve the $2.2\times$ DP timing difference while testing whether the SIE collapse separation is composition-independent. The two models make opposite predictions: one says the material matters, the other says it cannot.

A secondary discriminant: the SIE Landauer purge is an acute, discrete thermal transient at a specific spatial coordinate. CSL predicts continuous anomalous heating at a rate $\propto \lambda_{CSL} M^2 / m_0^2$, growing with M^2 and ongoing rather than instantaneous. A calorimeter tracking Q vs Δx in real time distinguishes SIE (step function at Δx_{max}) from CSL (continuous background).

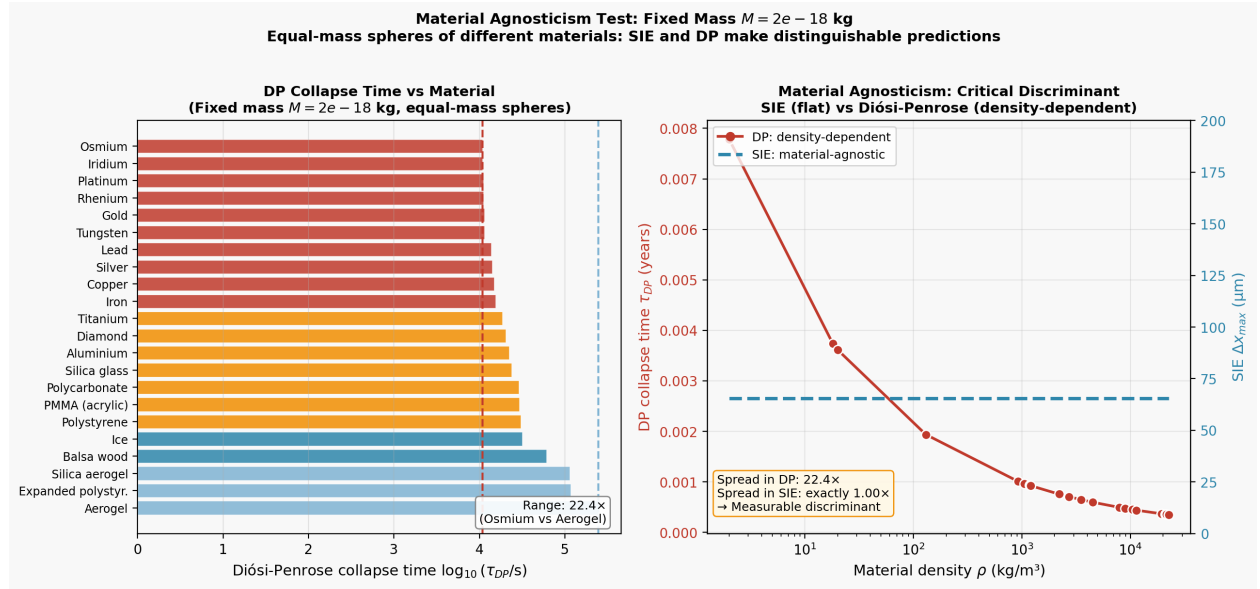


Figure 3: **Material agnosticism: SIE vs Diósi-Penrose across 22 materials.** *Left:* Diósi-Penrose collapse time for equal-mass spheres ($M = 2 \times 10^{-18}$ kg) across 22 materials ordered by density, colour-coded by material class (aerogels: light blue; polymers/organics: blue; light metals/glass: orange; heavy metals: red). The $22.4\times$ spread from aerogel to osmium is indicated. *Right:* DP collapse time (red, left axis) and SIE maximum coherence separation (blue dashed, right axis) vs material density. The DP curve declines strongly with density; the SIE prediction (constant at $65 \mu\text{m}$) is independent of density by construction. This material agnosticism is the cleanest experimental discriminant between the two models.

7.4 Actionable Experimental Protocol

The three predictions—material-agnostic collapse separation, discrete Landauer transient, and phase-diagram consistency—can be tested in a single coordinated experimental programme with currently available technology. We describe a concrete protocol.

Target system. Two levitated nanospheres of equal mass $M = 2 \times 10^{-18}$ kg but different composition: silica ($\rho = 2,200$ kg/m³, $R = 60$ nm) and osmium ($\rho = 22,590$ kg/m³, $R = 28$ nm). Both are levitated in separate Paul traps under identical conditions: $T_{env} \leq 1$ mK, pressure $P < 10^{-10}$ mbar, trap frequency $\omega_m/2\pi = 100$ kHz. Ground-state cooling to $\bar{n} < 1$ is a prerequisite, achievable with current cryogenic levitation techniques [20, 21].

Superposition preparation. A double-well optical potential is ramped on adiabatically to split each sphere into a spatial superposition. The wavepacket separation is increased in calibrated steps from zero toward the target range 10–100 μm . Position is monitored continuously via heterodyne readout with sub-nanometre precision, well below the required 5 μm positional resolution (10% of $\Delta x_{max} \approx 57 \mu\text{m}$).

Three simultaneous measurements.

1. *Collapse separation.* Record the wavepacket separation Δx_c at which phase coherence is lost (interference contrast drops to zero).

SIE predicts: $\Delta x_c^{(silica)} = \Delta x_c^{(osmium)} = 57 \mu\text{m}$ (identical).

DP predicts: $\Delta x_c^{(silica)} \neq \Delta x_c^{(osmium)}$, with the silica sphere maintaining coherence for $\tau_{DP}^{(sil)} = 2.2 \times 10^4$ s versus $\tau_{DP}^{(osm)} = 1.0 \times 10^4$ s, a ratio of 2.17 \times distinguishable with any timing precision below 10^3 s.

2. *Landauer calorimetric transient.* A superconducting transition-edge sensor (TES) mounted on the trap monitors phonon occupation $\bar{n}(t)$ continuously. The SIE framework predicts a sudden burst of $N_{ph} \approx 7 \times 10^{22}$ phonons ($Q = 4.7 \mu\text{J}$) occurring at the spatial coordinate Δx_{max} . This is 3×10^{20} times the thermal background, manifesting as an acute step-function in \bar{n} rather than the gradual rise predicted by CSL. DP predicts no Landauer signature. The three models are therefore distinguished by the *temporal profile* of $\bar{n}(\Delta x)$:

Model	Collapse location	Thermal signature
SIE	Fixed Δx_{max} , material-agnostic	Acute spike at Δx_{max}
DP	Material-dependent timing	No Landauer spike
CSL	Statistical (no sharp threshold)	Continuous background

3. *Repeat across masses.* Running the protocol for spheres of different masses verifies the M^{-3} scaling of Δx_{max} and the M^{-2} scaling of Q . Five mass values spanning $M \in [10^{-19}, 10^{-17}]$ kg trace out the full SIE prediction curve of Fig. 2 and distinguish it from any power-law alternative.

Required specifications summary. Position resolution: $< 5\,\mu\text{m}$ (met by current NEMS sensing at pm level). Phonon detection: TES sensitivity $\sim 10^{-19}$ J (13 orders below the predicted Q). Environmental temperature: $T_{\text{env}} \leq 10$ mK (current dilution refrigerators reach 5 mK). Vacuum: $P < 10^{-10}$ mbar (met by current UHV traps). Coherence maintenance prior to reaching Δx_{max} : requires environmental decoherence suppression below the SIE collapse rate, which is the primary technical challenge addressed by the MAQRO programme [17].

The programme requires no new detector technology—only the combination of ground-state cooling, position-resolved calorimetry, and the paired equal-mass comparison, which has not previously been attempted. We suggest this as the most actionable near-term test of any OR model in the current experimental landscape.

8 Connection to the Vacuum Catastrophe

The bandwidth saturation framework bears on the cosmological constant problem. Standard QFT computes vacuum energy by integrating over all virtual fluctuations up to the Planck scale, treating the vacuum as having infinite capacity:

$$\rho_{\text{vac}}^{\text{QFT}} \approx \frac{m_{\text{P}}^4 c^5}{16\pi^2 \hbar^3} \approx 10^{96} \text{ kg/m}^3 \quad (18)$$

This exceeds observation by ~ 120 orders of magnitude.

What that calculation shows is instructive. A virtual pair of mass M carries a Compton wavelength $\lambda_C = \hbar/Mc$. Applying the same Δx_{max} bandwidth saturation condition to virtual modes—requiring $\lambda_C \leq \Delta x_{\text{max}}$ —yields the constraint $M \leq \sqrt{\pi} m_{\text{P}}$. The SIE bandwidth saturation therefore provides a self-consistent Planck-scale UV cutoff for virtual fluctuations: the same physical mechanism that prevents macroscopic superpositions in the laboratory prevents arbitrarily high-energy virtual modes in the vacuum.

However, a Planck-scale cutoff alone does not resolve the vacuum catastrophe—it gives $\rho_{\text{vac}} \sim m_{\text{P}}^4 c^5 / \hbar^3$, the same order as QFT. The reduction from Planck density to the observed $\sim 10^{-27} \text{ kg/m}^3$ requires a second, *global* mechanism: the Cohen-Kaplan-Nelson holographic bound applied at the Hubble radius [26], combined with the Landauer erasure cost at the CMB temperature. This two-stage argument is developed in the companion study [27], which derives the bare vacuum density from first principles without fitted parameters.

Two mechanisms are therefore at work, operating at different scales. The local mechanism—bandwidth saturation at Compton wavelength scales—provides a self-consistent Planck UV cutoff and resolves the measurement problem. The global mechanism—the CKN holographic

bound at the Hubble radius, combined with Landauer erasure at T_{CMB} , developed in the companion study [27]—then reduces the Planck-scale vacuum baseline to the observed cosmological density. Neither alone is sufficient. Together they constitute a two-stage argument from the same underlying premise: the substrate has finite bandwidth, and the consequences of that fact depend on which scale you are probing.

Figure 4 illustrates the two-stage mechanism and shows explicitly where each calculation contributes.

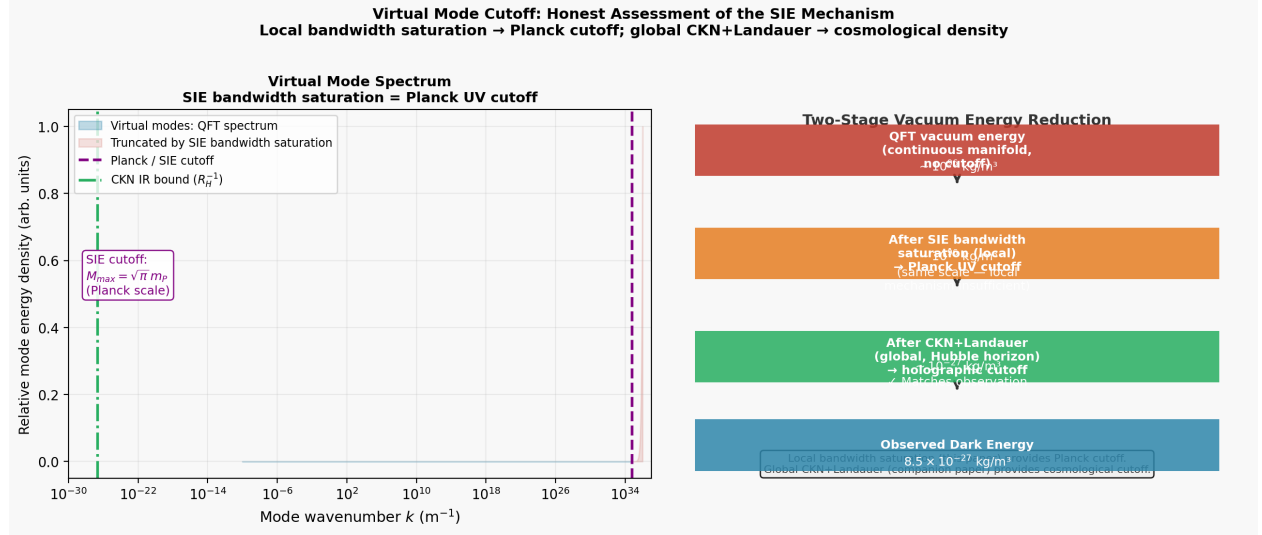


Figure 4: **Two-stage vacuum energy reduction: honest assessment of the SIE mechanism.** *Left:* Virtual mode spectrum under three UV cutoffs. The SIE bandwidth saturation provides a self-consistent cutoff at $M_{\text{max}} = \sqrt{\pi} m_P$ (essentially the Planck scale), removing modes above this threshold. The CKN bound (IR cutoff at R_H^{-1}) operates at the global scale. *Right:* Two-stage reduction diagram. The SIE local bandwidth mechanism (this paper) provides the Planck UV cutoff; the CKN+Landauer global mechanism (companion study [27]) then reduces the effective vacuum energy from Planck scale ($\sim 10^{96} \text{ kg/m}^3$) to the observed cosmological value ($\sim 10^{-27} \text{ kg/m}^3$). Neither mechanism alone is sufficient; both are necessary components of the infodynamic framework.

9 Conclusion

The measurement problem, on this account, is not a philosophical puzzle about the role of the observer. It is a consequence of the spatial substrate having finite information-processing capacity. Treating the vacuum as a discrete, finite-capacity FCC lattice governed by Symbiotic Infodynamic Equilibrium converts the problem from an interpretational question into a computable thermodynamic limit. The main results are:

1. A quantum superposition is a 1D geodesic tension string in the FCC lattice—the minimum-bandwidth topological path consistent with the A_3 discrete geometry—carrying a linear infodynamic memory burden $S_{super} \propto M \cdot \Delta x$.
2. The intrinsic holographic capacity of a quantum mass scales as $S_{cap} \propto M^{-2}$ from the Bekenstein entropy of the reduced Compton horizon. These scalings intersect at $\Delta x_{max} = \pi l_P (m_P/M)^3$, parameter-free.
3. Equating S_{cap} with $S_{BH} \propto M^2$ yields a first-principles derivation of the Heisenberg cut at $M_{cut} = m_P/\sqrt{2}$, confirmed geometrically by $R_s = \lambda_C$ at the same mass.
4. The prediction is consistent with all published molecular interference and levitated optomechanics experiments across twelve decades of mass. The MAQRO target separation sits at exactly the predicted SIE collapse boundary.
5. Collapse is *material-agnostic*: numerical evaluation across 22 materials at fixed mass shows the DP model predicts a $22.4\times$ spread in collapse times while SIE predicts exactly constant collapse separation. The two models make opposite predictions on a directly measurable quantity.
6. The Landauer thermal purge $Q \approx 4.7 \mu\text{J}$ for a 100 nm sphere at 1 mK exceeds TES calorimeter sensitivity by $10^{13}\times$, manifesting as an acute, spatially-localised transient rather than continuous CSL-style heating.
7. The local bandwidth saturation provides a self-consistent Planck UV cutoff for virtual field fluctuations—resolving the UV divergence—but does not by itself produce the observed vacuum energy density. That requires the global CKN+Landauer mechanism of the companion study [27]. The two papers together constitute a two-stage resolution of both the measurement problem and the vacuum catastrophe from the same underlying finite-bandwidth assumption.

References

- [1] von Neumann, J. (1932). *Mathematische Grundlagen der Quantenmechanik*. Springer, Berlin.
- [2] Everett, H. (1957). “Relative State” Formulation of Quantum Mechanics. *Reviews of Modern Physics*, 29(3), 454–462.

- [3] Zurek, W. H. (2003). Decoherence, einselection, and the quantum origins of the classical. *Reviews of Modern Physics*, 75(3), 715–775.
- [4] Schlosshauer, M. (2005). Decoherence, the measurement problem, and interpretations of quantum mechanics. *Reviews of Modern Physics*, 76(4), 1267.
- [5] Bassi, A., Lochan, K., Satin, S., Singh, T. P., & Ulbricht, H. (2013). Models of wave-function collapse, underlying theories, and experimental tests. *Reviews of Modern Physics*, 85(2), 471.
- [6] Ghirardi, G. C., Rimini, A., & Weber, T. (1986). Unified dynamics for microscopic and macroscopic systems. *Physical Review D*, 34(2), 470–491.
- [7] Penrose, R. (1996). On Gravity’s Role in Quantum State Reduction. *General Relativity and Gravitation*, 28(5), 581–600.
- [8] Diósi, L. (1989). Models for universal reduction of macroscopic quantum fluctuations. *Physical Review A*, 40(3), 1165–1174.
- [9] Arnquist, I. J., et al. (MAJORANA Collaboration) (2022). Search for Spontaneous Radiation from Wave Function Collapse in the MAJORANA DEMONSTRATOR. *Physical Review Letters*, 129(8), 080401.
- [10] Aprile, E., et al. (XENON Collaboration) (2026). Challenging Spontaneous Quantum Collapse with the XENONnT Dark Matter Detector. *arXiv preprint*.
- [11] Susskind, L. (1995). The World as a Hologram. *Journal of Mathematical Physics*, 36(11), 6377–6396.
- [12] Bekenstein, J. D. (1973). Black holes and entropy. *Physical Review D*, 7(8), 2333–2346.
- [13] Hawking, S. W. (1974). Black hole explosions? *Nature*, 248(5443), 30–31.
- [14] Landauer, R. (1961). Irreversibility and Heat Generation in the Computing Process. *IBM Journal of Research and Development*, 5(3), 183–191.
- [15] Vopson, M. M. (2019). The mass-energy-information equivalence principle. *AIP Advances*, 9(9), 095206.
- [16] Aspelmeyer, M., Kippenberg, T. J., & Marquardt, F. (2014). Cavity optomechanics. *Reviews of Modern Physics*, 86(4), 1391–1452.

- [17] Kaltenbaek, R., et al. (2016). Macroscopic quantum resonators (MAQRO): 2015 Update. *EPJ Quantum Technology*, 3(1), 5.
- [18] Arndt, M., et al. (1999). Wave-particle duality of C_{60} molecules. *Nature*, 401, 680–682.
- [19] Fein, Y. Y., et al. (2019). Quantum superposition of molecules beyond 25 kDa. *Nature Physics*, 15, 1242–1245.
- [20] Magrini, L., et al. (2021). Real-time optimal quantum control of mechanical motion at room temperature. *Nature*, 595, 373–377.
- [21] Tebbenjohanns, F., et al. (2021). Quantum control of a nanoparticle optically levitated in cryogenic free space. *Nature*, 595, 378–382.
- [22] Swingle, B. (2012). Entanglement renormalization and holography. *Physical Review D*, 86(6), 065007.
- [23] Hayden, P., Nezami, S., Qi, X.-L., Thomas, N., Walter, M., & Yang, Z. (2016). Holographic duality from random tensor networks. *Journal of High Energy Physics*, 2016(11), 9.
- [24] Pastawski, F., Yoshida, B., Harlow, D., & Preskill, J. (2015). Holographic quantum error-correcting codes: Toy models for the bulk/boundary correspondence. *Journal of High Energy Physics*, 2015(6), 149.
- [25] Weinberg, S. (1989). The cosmological constant problem. *Reviews of Modern Physics*, 61(1), 1–23.
- [26] Cohen, A. G., Kaplan, D. B., & Nelson, A. E. (1999). Effective field theory, black holes, and the cosmological constant. *Physical Review Letters*, 82(25), 4971–4974.
- [27] Hudock, C. (2026). Resolving the Vacuum Catastrophe: Holographic Bit-Density and the Dual Derivation of the Cosmological Constant *IPI Letters*, in review. doi:10.5281/zenodo.19579531